

# Efficient Water Electrolysis Using $\text{Ni}_2\text{P}$ as a Bifunctional Catalyst: Unveiling the Oxygen Evolution Catalytic Properties of $\text{Ni}_2\text{P}$

Lucas-Alexandre Stern<sup>§</sup> and Xile Hu\*

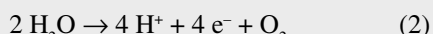
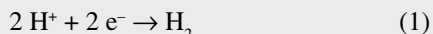
<sup>§</sup>SCS-DSM Award for best poster presentation in Catalysis Science and Engineering

**Abstract:** The excellent bifunctional catalytic activity of nickel phosphide ( $\text{Ni}_2\text{P}$ ) for water splitting is reported.  $\text{Ni}_2\text{P}$ , an active hydrogen evolving catalyst, is shown to be highly active for oxygen evolution. Only 290 mV of overpotential is required to generate a current density of  $10 \text{ mA cm}^{-2}$  in 1 M KOH. Under oxygen evolving conditions,  $\text{Ni}_2\text{P}$  undergoes structural modification to form a  $\text{Ni}_2\text{P}/\text{NiO}_x$  core-shell assembly, the catalytic active species.  $\text{Ni}_2\text{P}$  is applied on both electrodes of an alkaline electrolyser and a current density of  $10 \text{ mA cm}^{-2}$  is generated at 1.63 V.

**Keywords:** Electrochemistry · Janus catalyst ·  $\text{Ni}_2\text{P}$  · Oxygen evolution · Water splitting

## 1. Introduction

Global scale exploitation of renewable energy resources, such as wind and solar energy, demands efficient energy storage techniques. Electrochemical water splitting is one of the most attractive method for energy storage.<sup>[1]</sup> Water splitting is subdivided in two half-reactions, namely, the hydrogen evolution reaction (HER, Eqn. (1)) and the oxygen evolution reaction (OER, Eqn. (2)).



splitting catalysts have been developed, only few materials are able to catalyse both HER and OER in the same media. Bifunctional catalysts made from Earth-abundant metals would facilitate production and implementation of electrolyser devices. The reported bifunctional systems include Co,<sup>[2]</sup> Ni,<sup>[3]</sup> Cu,<sup>[4]</sup> NiFe LDH,<sup>[5]</sup> NiFeO<sub>x</sub>,<sup>[6]</sup> NiCo<sub>2</sub>S<sub>4</sub>,<sup>[7]</sup> Ni<sub>5</sub>P<sub>4</sub>,<sup>[8]</sup> CoO<sub>x</sub>,<sup>[9]</sup> CoP,<sup>[10]</sup> FeP.<sup>[11]</sup> In this article, we show that  $\text{Ni}_2\text{P}$ , an active HER catalyst, is efficient for the oxygen evolution reaction in alkaline medium. Under OER conditions, the material forms a  $\text{Ni}_2\text{P}/\text{NiO}_x$  core-shell heterostructure. This assembly generates a current density of  $10 \text{ mA cm}^{-2}$  at an overpotential of only 290 mV.<sup>[12]</sup> The Janus behaviour of the material permits the fabrication of an efficient alkaline electrolyser using  $\text{Ni}_2\text{P}$  as catalyst for both the cathode and the anode.

## 2. Oxygen Evolution Activity of $\text{Ni}_2\text{P}$

The  $\text{Ni}_2\text{P}$  nanoparticles were prepared via a solid-state thermal reaction previously reported by our group.<sup>[13]</sup> Briefly, a phosphorus source,  $\text{NaH}_2\text{PO}_2$  (0.66 g, for analysis, Acros), and a nickel salt,  $\text{NiCl}_2 \cdot 6\text{H}_2\text{O}$  (0.3 g, ReagentPlus®, Aldrich), were ground together at ambient atmosphere and then placed in a quartz boat. This was then transferred into a tubular furnace and heated at 250 °C under a constant flow of nitrogen. The obtained powder was further ground and the impurities were washed off from the product using copious amount of distilled water. The product was then dried in an oven at 50 °C for a few hours. X-ray diffraction of the obtained powder is shown in Fig. 1b. The diffraction signal was compared

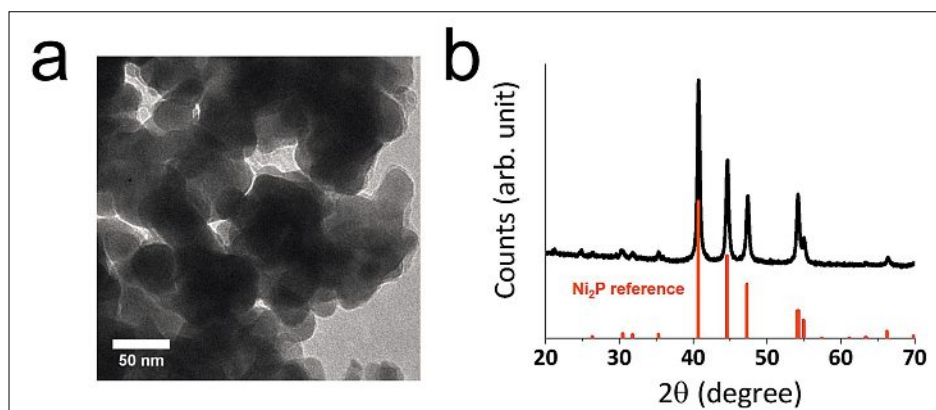


Fig. 1. a) TEM image of polycrystalline  $\text{Ni}_2\text{P}$ . b) Powder X-ray diffraction pattern of the  $\text{Ni}_2\text{P}$  nanoparticles. Adapted by permission of The Royal Society of Chemistry from ref. [12].

\*Correspondence: Prof. Dr. X. Hu  
Laboratory of Inorganic Synthesis and Catalysis  
Institute of Chemical Sciences and Engineering  
École Polytechnique Fédérale de Lausanne (EPFL)  
ISIC-LSCI, BCH 3305  
CH-1015 Lausanne  
E-mail: xile.hu@epfl.ch

to the reference diffraction pattern obtained from the International Center of Diffraction Data. The overlapping signals indicated the successful synthesis of pure phase  $\text{Ni}_2\text{P}$ . The transmission electron microscopy (TEM) image shows that the  $\text{Ni}_2\text{P}$  nanoparticles have an averaged size of 50 nm and are coated with a thin amorphous layer (Fig. 1a).

To evaluate the catalytic activity of  $\text{Ni}_2\text{P}$  for the oxygen evolution reaction, linear sweep voltammetry scans were performed in 1 M KOH. The catalytic activity of nickel phosphide was measured and compared to various nanomaterials including  $\text{IrO}_2$ , Ni,  $\text{NiO}_x$  and an electrodeposited  $\text{Ni(OH)}_2$  film (Fig. 2a).  $\text{IrO}_2$  (99.9% Ir, aber) and  $\text{NiO}_x$  (99.8% trace metals basis, Aldrich) were used as received, while Ni nanoparticles and  $\text{Ni(OH)}_2$  film preparation has been reported previously.<sup>[14]</sup> The loading of  $\text{IrO}_2$ , Ni,  $\text{NiO}_x$  applied on the glassy carbon electrode was identical to  $\text{Ni}_2\text{P}$  loading. Fig. 2a shows that  $\text{Ni}_2\text{P}$  nanoparticles catalytic activity is superior to that of the different catalysts evaluated. The overpotential to generate a current density of  $10 \text{ mA cm}^{-2}$  is only 290 mV for  $\text{Ni}_2\text{P}$ . To reach similar current density,  $\text{IrO}_2$  and  $\text{Ni(OH)}_2$  requires an additional 40 mV of overpotential compared to  $\text{Ni}_2\text{P}$ . Ni and  $\text{NiO}_x$  drive a current density of  $10 \text{ mA cm}^{-2}$  at 365 mV of overpotential.

The electrochemical surface area (ESCA) of the materials was assessed and compared. For this purpose, the double-layer capacitance of the materials was calculated. Fig. 2b shows the ESCA of the nickel-based catalysts. The ESCA for the different materials were expressed in terms of surface averaged double layer capacitance.  $\text{Ni}_2\text{P}$  have higher surface area for similar loading than other nickel materials:  $176.9 \mu\text{F cm}^{-2}$ , followed by  $\text{Ni(OH)}_2$   $137.2 \mu\text{F cm}^{-2}$ .  $\text{NiO}_x$  and Ni nanoparticles have smaller ESCA values  $68$  and  $37 \mu\text{F cm}^{-2}$  respectively. The correlation determined between the ESCA of Ni,  $\text{NiO}_x$ ,  $\text{Ni(OH)}_2$  and their respective catalytic activity at the fixed overpotential of 325 mV cannot be applied to  $\text{Ni}_2\text{P}$ . This indicates that high surface area is not the sole reason for the superior catalytic activity of nickel phosphide.

The stability of the nickel phosphide nanoparticles was probed by galvanostatic experiment. Fig. 2c shows that the overpotential to generate  $10 \text{ mA cm}^{-2}$  increased only of 10 mV over the course of 10 hours indicating high stability of the catalyst. The nickel phosphide oxygen evolution activity was also compared to several state-of-the-art materials (Table 1). It can be seen that  $\text{Ni}_2\text{P}$  is more active than many Ni and Co-based oxides, and even  $\text{IrO}_2$  in base.

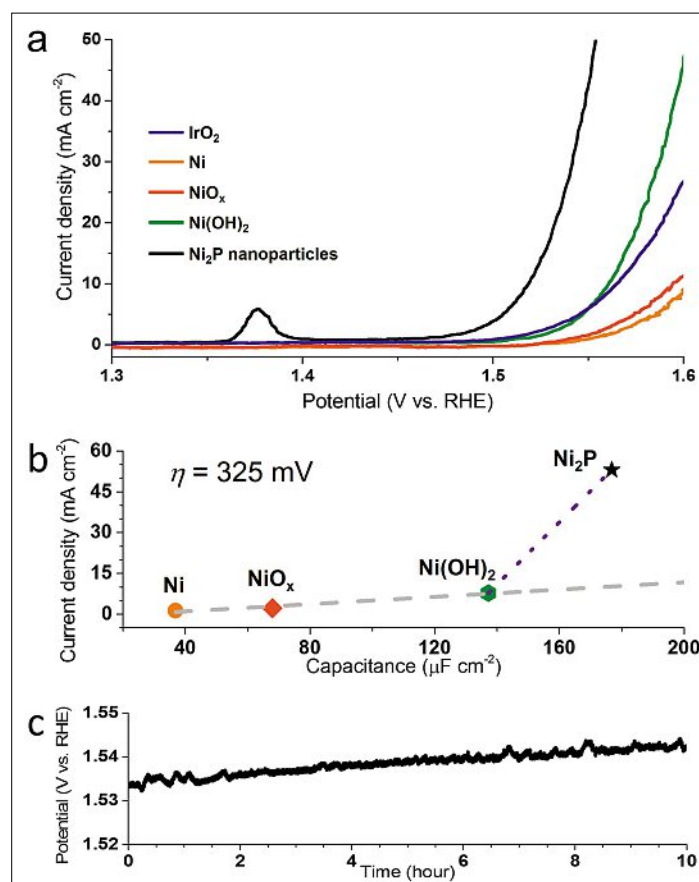


Fig. 2. a) Linear sweep voltammetric (LSV) curves of  $\text{Ni}_2\text{P}$ , Ni nanoparticles,  $\text{NiO}_x$  nanoparticles, electrodeposited  $\text{Ni(OH)}_2$ , and  $\text{IrO}_2$  in 1 M KOH. b) Correlation of the current density at an overpotential of 325 mV, with the electrochemical capacitance of the different nickel materials. c) Galvanostatic measurement on the  $\text{Ni}_2\text{P}$  nanoparticles in 1 M KOH at a constant current density of  $10 \text{ mA cm}^{-2}$  over 10 h. Conditions: pretreated working electrode, pre-activated  $\text{Ni}_2\text{P}$  catalysts,  $5 \text{ mV s}^{-1}$ ,  $0.14 \text{ mg cm}^{-2}$ . Adapted by permission of The Royal Society of Chemistry from ref. [12].

Table 1. Comparison of the OER catalytic activity of state-of-the-art catalysts. Adapted by permission of The Royal Society of Chemistry from ref. [12].

Material	Loading [ $\text{mg cm}^{-2}$ ]	$\eta @ 10 \text{ mA cm}^{-2}$ [mV]	Ref.
Ni	0.14	377	This work
$\text{NiO}_x$	0.14	364	This work
$\text{Ni(OH)}_2$	0.14	331	This work
$\text{Ni}_2\text{P}$	0.14	290	This work
$\text{NiO}_x$	0.02	360	[15c]
$\alpha\text{-Ni(OH)}_2$	0.20	331	[15d]
$\beta\text{-Ni(OH)}_2$	0.20	444	[15d]
$\text{NiCo}_2\text{O}_4$	0.53	565	[15e]
$\text{NiFe-LDH}$	0.20	320	[16]
$\text{CoO}_x@\text{CN}$	0.42	410	[9]
BSCF82	0.25	320	[17]
$\text{IrO}_2$	-	320	[15b]
$\text{IrO}_2^a$	0.35	275	[18]

<sup>a</sup>Catalytic activity measured in acidic conditions

### 3. $\text{Ni}_2\text{P}/\text{NiO}_x$ Core-shell Structure: The OER Catalytic Active Species

To identify the nature of the chemical modifications undergone by nickel phosphide during water oxidation, the

$\text{Ni}_2\text{P}$  nanoparticles were characterized prior and after catalysis by high-resolution TEM, energy-dispersive X-ray element mapping and X-ray photoelectron spectroscopy (XPS) (Fig. 3). The data indicate that prior to catalysis crystalline

nanoparticles of  $\text{Ni}_2\text{P}$  are embedded in an amorphous matrix, which is oxygen-rich, contains phosphorus, and is free of any metallic content (Fig. 3a–e). This layer likely consists of residual  $\text{P}_2\text{O}_5$  as a side product of the catalyst synthesis. Important structural change can be observed on the catalytic material after oxygen evolution for 1 h. The HRTEM image (Fig. 3g) shows that after OER, the layer surrounding the nanoparticles is composed of ultrafine particles of about 2–3 nm diameter. Closer inspection of the particles in the layer revealed the presence of lattice registry indicative of crystalline materials. Fast Fourier transform (FFT) (Fig. 3g inset) allowed measurement of the crystal lattice spacing of the fine particles. The distance between two crystal planes is characteristic of  $\text{NiO}_x$  material. A crystal lattice spacing of the material's core was also determined and it is characteristic of the (100) facet of  $\text{Ni}_2\text{P}$ . Elemental mapping images of the catalyst after OER (Fig. 3h–k) clearly show the  $\text{Ni}_2\text{P}/\text{NiO}_x$  core-shell heterostructure that the material adopts under oxidative conditions. Nickel is present in both layers of the material. Oxygen coats homogeneously the particle surface. Phosphorus is present only in the core. The structure of the material was further corroborated by XPS measurements (Fig. 3l).<sup>[19]</sup> Electrochemical measurements also validate the formation of a  $\text{Ni}_2\text{P}/\text{NiO}_x$  core-shell heterostructure during OER. The oxidation peak observed is indicative of the  $\text{Ni}^{2+}/\text{Ni}^{3+}$  oxidation in many nickel oxide hydroxide and bimetallic  $\text{NiFeO}_x$  OER catalysts.<sup>[13,15a,15d,20]</sup> The pre-activation of the catalyst is, thus, hypothesized to allow the *in situ* formation of a stable  $\text{Ni}_2\text{P}/\text{NiO}_x$  core-shell heterostructure with improved OER catalytic properties.

The enhanced catalytic activity of the  $\text{Ni}_2\text{P}/\text{NiO}_x$  core-shell structure compared to other  $\text{NiO}_x$  catalysts for OER has two possible origins. On one hand the unique assembly provides significant improvement in electron conduction.<sup>[21]</sup> Indeed, the metallic  $\text{Ni}_2\text{P}$  core might provide an efficient electron pathway to the insulating  $\text{NiO}_x$  shell. On the other hand,  $\text{Ni}_2\text{P}$  allows the *in situ* formation of ultrafine nanoparticles of  $\text{NiO}_x$ , which allows higher active site exposure. Synergistic effects, which warrant further investigation, may play a role as well.

#### 4. Efficient and Inexpensive Alkaline Electrolyser Fabricated Using $\text{Ni}_2\text{P}$ as Catalyst

The hydrogen evolving capabilities of  $\text{Ni}_2\text{P}$  have been reported recently.<sup>[13,22]</sup> Given the presented OER catalytic activity, an alkaline electrolyser using  $\text{Ni}_2\text{P}$  as both

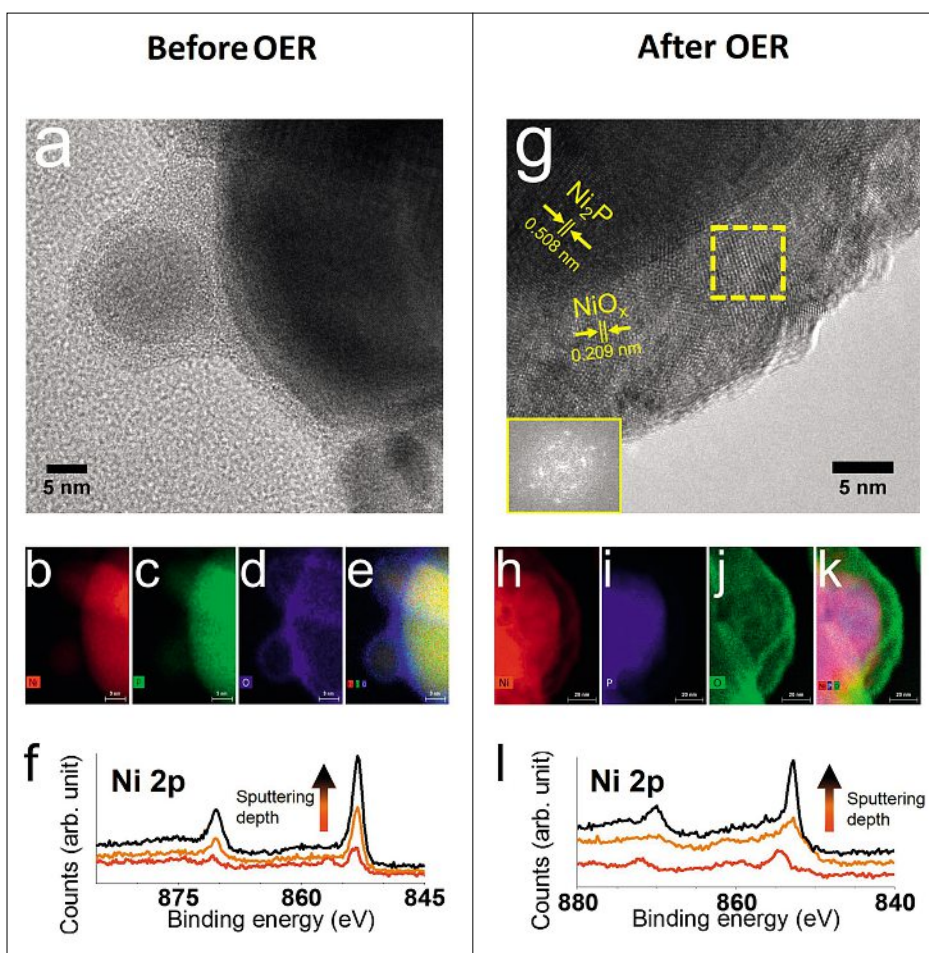


Fig. 3. a) High-resolution TEM (HRTEM) image of the  $\text{Ni}_2\text{P}$  nanoparticles prior to oxygen evolution catalysis. b–e) Corresponding energy dispersive X-ray (EDX) elemental maps of the system prior to catalysis (scale bar: 9 nm). b) Ni elemental mapping. c) Phosphorus elemental mapping. d) Oxygen elemental mapping. e) Combined elemental mapping. f) High-resolution depth-profiling XPS spectra of the Ni 2p area. As the profiling depth increases (arrow direction), the FWHM decreases, indicative of stronger metallic Ni content. g) HRTEM image of the  $\text{Ni}_2\text{P}$  nanoparticles after electrochemical pretreatment at 1.5 V vs. RHE for one hour. Inset (lower left): FFT of the framed area (middle). The spots observed on the FFT are indicative of registry order and so of crystallinity. The lattice fringes spacing of the materials were determined using FFT. They correspond to the characteristic (100) facet of  $\text{Ni}_2\text{P}$  and specific facets of nickel oxides/hydroxides species,  $\text{NiO}_x$ . h–k) Corresponding EDX maps of the elements on the sample region shown in (g) (scale bar: 20 nm). h) Nickel elemental mapping. i) Phosphorus elemental mapping. j) Oxygen elemental mapping. k) Combined elemental mapping of Ni, O, and P. l) High-resolution depth-profiling XPS spectra of the Ni 2p area after catalytic activity. As the profiling depth increases (arrow direction), the large FWHM, that is indicative of nickel oxide species, decreases, indicative of stronger metallic Ni content. This confirms the presence of a surface oxide layer around metallic nickel phosphide core. Adapted by permission of The Royal Society of Chemistry from ref. [12].

cathode and anode catalyst was fabricated. The catalyst support used for this device was nickel foam. The loading of catalyst applied on the two Ni foams was  $10 \text{ mg cm}^{-2}$ . Fig. 4 shows the measured catalytic activity of the alkaline electrolyser in 1 M KOH. The activity is compared with bare Ni foams as reference. To generate a current density of  $10 \text{ mA cm}^{-2}$  the alkaline electrolyser employing  $\text{Ni}_2\text{P}$  as catalyst only requires 400 mV of overpotential while bare Ni foams demands 560 mV of overpotential to reach the same value of current density.<sup>[12]</sup> During water electrolysis, the cathode and the anode were separated using a glass frit membrane to avoid any undesirable

reactions. The stability of the alkaline electrolyser was tested *via* galvanostatic measurement. A constant current density of  $10 \text{ mA cm}^{-2}$  was applied for 10 h. Fig. 4 inset shows that the overpotential hardly increases during the course of the experiment and indicates high stability of the fabricated electrolyser. To confirm that all the current generated results from water splitting, the total pressure increase due to hydrogen and oxygen evolution was recorded using a pressure sensor during the electrochemical measurement. The pressure sensor data allows the amount of gas evolved to be calculated over the course of the water electrolysis. The

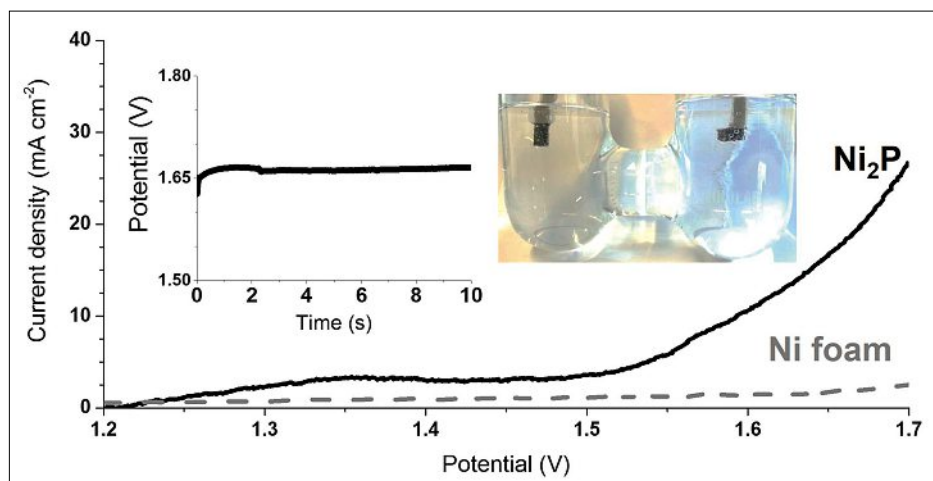


Fig. 4. LSV to evaluate the alkaline electrolyser activity under gas separating conditions. The Ni<sub>2</sub>P system (loading 10 mg cm<sup>-2</sup>, activated anode) necessitates only 400 mV to generate 10 mA cm<sup>-2</sup>. The Ni foam support was evaluated under similar conditions (gas separation, activated anode but without catalyst) and required 560 mV to generate 10 mA cm<sup>-2</sup>. A galvanostatic experiment on the Ni<sub>2</sub>P alkaline electrolyser with glass frit separation was performed (inset) and indicates the good stability of the system over 10 hours of electrolysis at 10 mA cm<sup>-2</sup>. An optical photograph illustrates the cell used for these experiments. Adapted by permission of The Royal Society of Chemistry from ref. [12].

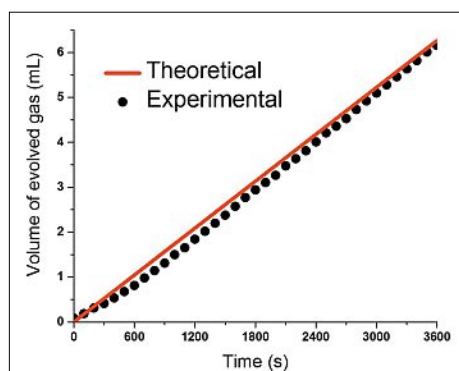


Fig. 5. Faraday yield measurement of the alkaline electrolyser fabricated from Ni<sub>2</sub>P loaded Ni foams (loading 10 mg cm<sup>-2</sup>). The quantity of gas evolved was determined by a pressure sensor. The overlapping lines between the theoretical and experimental values indicate a quantitative Faraday yield of the system, after an induction period of about 250 s. During this induction period, the gas generated are dissolved in the solution to reach an equilibrium. After the induction period, the gas generated can be measured by the pressure sensor. The galvanostatic experiment was performed over 1 h at a constant current density of 10 mA cm<sup>-2</sup>. The anode was activated prior the galvanostatic experiment. The cathode was used as it is. Adapted by permission of The Royal Society of Chemistry from ref. [12].

theoretical volume of gas evolved can then be calculated by determining the charge passed over the course of the experiment. Comparison between experimental and theoretical volume of gas determines then

the Faradaic efficiency of the alkaline electrolyser. Fig. 5 illustrates that the experimental and theoretical amount of gas evolved overlaps indicative of a quantitative Faraday efficiency for the device. Ni<sub>2</sub>P is thus an active and stable bifunctional catalyst for water splitting in alkaline media.

## 5. Conclusion

In summary, Ni<sub>2</sub>P is an active catalyst for OER in alkaline conditions. The catalyst is prepared *via* a simple solid-state reaction from abundant and cheap reagents. The catalytic active species is a Ni<sub>2</sub>P/NiO<sub>x</sub> core-shell heterostructure that is formed *in situ* under OER conditions. The catalytic activity is superior to several state-of-the-art catalysts. The Janus behaviour of the catalyst allows the fabrication of an efficient alkaline electrolyser who generates 10 mA cm<sup>-2</sup> at an overpotential of only 400 mV. Ni<sub>2</sub>P shows promise of potential applications for future devices and highlights the potential of Earth-abundant catalysts as viable electrocatalysts for energy conversion devices and fuel cell applications.

## Acknowledgement

This work is supported by the EPFL. We thank Dr. Ligang Feng and Dr. Fang Song at EPFL for assistance in the experiments.

Received: December 1, 2015

- [1] N. S. Lewis, D. G. Nocera, *Proc. Natl. Acad. Sci. USA* **2006**, *103*, 15729.
- [2] S. Cobo, J. Heidkamp, P.-A. Jacques, J. Fize, V. Fourmond, L. Guetaz, B. Jousselme, V. Ivanova, H. Dau, S. Palacin, M. Fontecave, V. Artero, *Nat. Mater.* **2012**, *11*, 802.
- [3] C. He, X. Wu, Z. He, *J. Phys. Chem. C* **2014**, *118*, 4578.
- [4] X. Liu, H. Zheng, Z. Sun, A. Han, P. Du, *ACS Catal.* **2015**, *5*, 1530.
- [5] J. Luo, J.-H. Im, M. T. Mayer, M. Schreier, M. K. Nazeeruddin, N.-G. Park, S. D. Tilley, H. J. Fan, M. Graetzel, *Science* **2014**, *345*, 1593.
- [6] H. Wang, H.-W. Lee, Y. Deng, Z. Lu, P.-C. Hsu, Y. Liu, D. Lin, Y. Cui, *Nat. Commun.* **2015**, *6*, 7261.
- [7] D. Liu, Q. Lu, Y. Luo, X. Sun, A. M. Asiri, *Nanoscale* **2015**, *7*, 15122.
- [8] M. Ledendecjer, S. K. Calderón, C. Papp, H.-P. Steinrück, M. Antonietti, M. Shalom, *Angew. Chem. Int. Ed.* **2015**, *54*, 12361.
- [9] H. Jin, J. Wang, D. Su, Z. Wei, Z. Pang, Y. Wang, *J. Am. Chem. Soc.* **2015**, *137*, 2688.
- [10] a) N. Jiang, B. You, M. Sheng, Y. Sun, *Angew. Chem. Int. Ed.* **2015**, *54*, 6251; b) Y. Yang, H. Fei, G. Ruan, J. M. Tour, *Adv. Mater.* **2015**, *27*, 3175; c) J. Chang, Y. Xiao, M. Xiao, J. Ge, C. Liu, W. Xing, *ACS Catal.* **2015**, *5*, 6874.
- [11] Y. Yan, B. Y. Xia, X. Ge, Z. Liu, A. Fisher, X. Wang, *Chem. Eur. J.* **2015**, *21*, 18062.
- [12] L.-A. Stern, L. Feng, F. Song, X. Hu, *Energy Environ. Sci.* **2015**, *8*, 2347.
- [13] L. Feng, H. Vrubel, M. Bensimon, X. Hu, *Phys. Chem. Chem. Phys.* **2014**, *16*, 5917.
- [14] a) Y. Chen, D.-L. Peng, D. Lin, X. Luo, *nanotechnol.* **2007**, *18*, 505703; b) D. A. Corrigan, R. M. Bendert, *J. Electrochem. Soc.* **1989**, *136*, 723.
- [15] a) L. Trotochaud, J. K. Ranney, K. N. Williams, S. W. Boettcher, *J. Am. Chem. Soc.* **2012**, *134*, 17253; b) C. C. L. McCrory, S. H. Jung, J. C. Peters, T. F. Jaramillo, *J. Am. Chem. Soc.* **2013**, *135*, 16977; c) K. Fominykh, J. M. Feckl, J. Sicklinger, M. Doeblinger, S. Boecklein, J. Ziegler, L. Peter, J. Rathousky, E.-W. Scheidt, T. Bein, D. Fattakhova-Rohlfing, *Adv. Funct. Mater.* **2014**, *24*, 3123; d) M. Gao, W. Sheng, Z. Zhuang, Q. Fang, S. Gu, J. Jiang, Y. Yan, *J. Am. Chem. Soc.* **2014**, *136*, 7077; e) H. Shi, G. Zhao, *J. Phys. Chem. C* **2014**, *118*, 25939.
- [16] M. Gong, Y. Li, H. L. Wang, Y. Y. Liang, J. Z. Wu, J. G. Zhou, J. Wang, T. Regier, F. Wie, H. J. Dai, *J. Am. Chem. Soc.* **2013**, *135*, 8452.
- [17] K. J. May, C. E. Carlton, K. A. Stoerzinger, M. Risch, J. Suntivich, Y.-L. Lee, A. Grimaud, Y. Shao-Horn, *J. Phys. Chem. Lett.* **2012**, *3*, 3264.
- [18] L. Ouattara, S. Fierro, O. Frey, M. Koudelka, C. Comninellis, *J. Appl. Electrochem.* **2009**, *39*, 1361.
- [19] P. E. R. Blanchard, A. P. Grosvenor, R. G. Cavell, A. Mar, *J. Mater. Chem.* **2009**, *19*, 6015.
- [20] a) R. L. Doyle, I. J. Godwin, M. P. Brandon, M. E. G. Lyons, *Phys. Chem. Chem. Phys.* **2013**, *15*, 13737; b) L.-A. Stern, X. Hu, *Faraday Discuss.* **2014**, *176*, 363.
- [21] a) M. Gong, W. Zhou, M.-C. Tsai, J. Zhou, M. Guan, M.-C. Lin, B. Zhang, Y. Hu, D.-Y. Wang, J. Yang, S. J. Pennycook, B.-J. Hwang, H. Dai, *Nat. Commun.* **2014**, *5*, 4695; b) G. Elmaci, C. E. Frey, P. Kurz, B. Zumreoglu-Karan, *Inorg. Chem.* **2015**, *54*, 2734; c) L. Trotochaud, S. L. Young, J. K. Ranney, S. W. Boettcher, *J. Am. Chem. Soc.* **2014**, *136*, 6744.
- [22] E. J. Popczun, J. R. McKone, C. G. Read, A. J. Biacchi, A. M. Wiltrout, N. S. Lewis, R. E. Schaak, *J. Am. Chem. Soc.* **2013**, *135*, 9267.